## Title

The Allosteric Regulation of Axial/Rhombic Population in a “Type 1” Copper Site: Multi-Edge X-ray Absorption Spectroscopic and Density Functional Studies of Pseudoazurin

## Permalink

https://escholarship.org/uc/item/7hz9030g

## Journal

Bulletin of the Chemical Society of Japan, 88(12)

## ISSN

0009-2673

## Authors

Yamaguchi, Takahide
Yano, Junko
Yachandra, Vittal K
et al.

## Publication Date

2015-12-15

## DOI

10.1246/bcsj.20150225

Peer reviewed

Selected Paper

# The Allosteric Regulation of Axial/Rhombic Population in a “Type 1” Copper Site: Multi-Edge X-ray Absorption Spectroscopic and Density Functional Studies of Pseudoazurin

**Takahide Yamaguchi,[1] Junko Yano,[2] Vittal K. Yachandra,[2] Yuko Nihei,[1] Hiromi Togashi,[1]**
**Robert K. Szilagyi,*[3] and Takamitsu Kohzuma*[1]**

[1]Institute of Applied Beam Science, Ibaraki University, 1-2-2 Bunkyo, Mito, Ibaraki 310-8512

[2]Physical Biosciences Division, Lawrence Berkeley National Laboratory, Berkeley, CA 94720, USA

[3]Department of Chemistry and Biochemistry, Montana State University, Bozeman, MT, 59717, USA

E-mail: kohzuma@mx.ibaraki.ac.jp

Received: June 29, 2015; Accepted: August 29, 2015; Web Released: September 4, 2015

**Takamitsu Kohzuma**
Takamitsu Kohzuma received Ph.D. from Kanazawa University in 1989, worked at Osaka University since 1989. He became an associate professor of Ibaraki University in 1994, and he has been a professor of Ibaraki University since 2004. His research interests are bioinorganic chemistry and weak chemical interaction in protein.

**Robert K. Szilagyi**
Robert K. Szilagyi received Ph.D. from University of Veszprem, Hungary in 1998. He worked as a postdoctoral fellow at University of Emory (1998–2000) and at Stanford University (2000–2003). Since 2009 he has been an associate professor of Montana State University. His research interests are computational chemistry, inorganic chemistry, and X-ray spectroscopy.

## Abstract

The co-existence of “axial” and “rhombic” coordination environments has been demonstrated in a “Type 1” copper site of Pseudoazurin. This observation opens up previously not considered interpretations for the relationship between geometry and electronic structure of the four coordinate copper site. The Met16 variants of pseudoazurin were considered as model systems for investigating the effect of weak interactions from the second coordination sphere. The correlation between geometric and electronic structures of “Type 1” copper site was evaluated by the multi-edge (Cu K-edge and S K-edge) X-ray absorption spectroscopy (XAS) of Met16 variants of pseudoazurin. The co-existing axial and rhombic sites in pseudoazurin were characterized by Cu–ligand distances, effective nuclear charge, and Cu–S(Cys) covalency from XAS. The XAS results were correlated with DFT calculations for investigating the effect of protein environment from the inner-sphere and beyond around the Cu site. The combined experimental and theoretical results support the presence of a close correlation between outer sphere environment and inner sphere coordination environment. This is achieved in pseudoazurin by a previously undisclosed allosteric effect that involves a rearrangement of the protein tertiary structure.

## Introduction

The biological role of blue and green copper proteins is electron transfer via Cu(I)/Cu(II) redox chemistry[1] in plants[2–5] and bacteria.[6–8] The metal binding site of blue copper protein is classified as “Type 1” copper due to characteristic spectroscopic signatures of the oxidized form.[9] Protein crystallography[10–17] has revealed a copper coordination sphere composed of conserved histidine and cysteine residues, and an axial ligand that can vary.[18] Met is the most common axial ligand in [$N_2S_2$] 4-coordinated “Type 1” copper site.[10,12,13,16,19] The other varieties of coordination are found as [$N_2SO$] in stellacyanin and mavicyanin, [$N_2S_2O$] in azurin and [$N_2S$] in laccase and ceruloplasmin.[14,15,20–22] Because of the diversity, the influence of axial ligands was a concern for the "Type 1" copper site.[23] The effects of the axial ligand were explored by comparison of native proteins,[24] mutation studies,[25–32] or computational studies.[33,34] For examples, the spectroscopic and electrochemical study of azurin Met121 variants with unnatural amino acid suggested hydrophobicity ($\log P$) to be a regulator of reduction potential of "Type 1" copper site.[26,27] Met182Thr variant of *Rhodobacter sphaeroides* nitrite reductase (NiR) shows great perturbation of the electronic structure of the Cu site.[28]

Plastocyanin (Pc)[35,36] and nitrite reductase from *Achoromobactor cycloclastes* (*Ac*NiR)[37] are the most studied blue and green copper proteins, respectively. Despite the compositionally identical "Type 1" site with [$N_2S_2$] ligand set, their reduction potentials differ considerably (Pc: 370 mV,[35] NiR: 260 mV[38]). Their electronic absorption spectra also differ in the absorbance ratio at 450 and 600 nm ($A_{450}/A_{600}$), which can be related to the presence of pure-π and mixed π/pseudo-σ Cu(II)–S(Cys) bonding in Pc[39] and NiR,[39] respectively. The spectral differences correlate with the different Cu coordination geometries.[16,17] Notably, the electronic structure and coordination geometry of cucumber basic protein (CBP) was found to be between those of Pc and NiR. This was explained by the presence of a continuous distortion coordinate between the green and blue sites driven by the Jahn–Teller distortion of the Cu site.[39,40] This explanation assumes the presence of a single Cu coordination environment in a "Type 1" site. Critically it lacks the possibility of protein backbone dynamics affecting the "Type 1" site. A very recent atomic resolution protein crystallography demonstrated the importance of protein main chain dynamics on the properties of redox active metal site for the example of Cytochrome *c′* Fe(III) containing metalloprotein.[41]

Pseudoazurin from *Achromobacter cycloclastes* (*Ac*PAz) is a member of the blue copper protein family with a conserved Met16 residue in the outer coordination sphere, approximately 5 Å away from the "Type 1" Cu site.[10] The effects of mutations at Met16 were interpreted in terms of a perturbation in the interaction between the 16th amino acid and His81, a ligand to the Cu site. For example, aromatic amino acid substitutions drastically affect the spectroscopic and electrochemical properties of the Cu site. This was rationalized by the appearance of a π–π stacking interaction between the aromatic residue in position 16 and His81.[42] The presence of stacking arrangement between Phe16 and His81 was confirmed by the crystal structure of Met16Phe variant.[43]

A series of Met16 variants of PAz manifested a systematic deviation of $A_{450}/A_{600}$ ratio relative to Pc, NiR and CBP. The interpretation of EPR spectra showed the possibility for the simultaneous existence of two copper sites corresponding to an axial (blue) and a rhombic (green) site.[42,44] Notably, this has already been implicated as an explanation of resonance Raman spectral differences of *Ac*NiR in 1988.[45] The coexistence of blue and green copper sites was also discussed in theoretical studies.[46–48] Moreover, the presence of two Cu sites in *Ac*NiR was related to a mixture of enthalpy favored rhombic and entropy favored axial site from thermodynamic data.[48,49] It was argued that (i) the entatic state and rack induced bonding are due to protein constraints imposed on coordinated Met axial ligand, thus preventing shorter Cu–S(Met) distance and prohibiting the formation of a green site in Pc and PAz from *Paracoccus pantrophus* (*Pp*PAz);[50] (ii) a thermal equilibrium of axial and rhombic populations in *Ac*NiR relative to Pc and *Pp*PAz is present due to lowered entatic state/rack induced bonding.[51]

For *Ac*PAz variants, the axial/rhombic populations are dependent on the outer-sphere composition with respect to the nature of 16th amino acid independently from temperature. The role of the non-covalent interactions, such as hydrogen bonding, ion–dipole network, π–π stacking interactions, and dispersion effects from the outer-sphere environment has already been implicated in perturbation of Cu site electronic structure.[12,42,44,52–54] We investigated here the experimental and theoretical coordination geometry of the Cu(II) site in a series of Met16 variants using X-ray absorption spectroscopic measurements and density functional theory (DFT) modeling. The combined experimental and computational results allowed us to propose an allosteric regulation of electronic structure of "Type 1" copper site in the presence of both axial and rhombic coordination environments.

X-ray absorption near-edge structure (XANES) and extended X-ray absorption fine structure (EXAFS) analyses are the two most common approaches to obtain structural information from X-ray absorption spectroscopic (XAS) data. XANES provides information about electronic structure, such as oxidation state or effective nuclear charge. EXAFS offers a glimpse of the local geometric structure via the radial distribution and number of neighboring atoms around an absorber.[55] Numerous XAS studies of blue copper protein have been reported to date.[24,30,39,56–60] The electronic structures with respect to Cu-based contributions, and Cu–ligand (Cu–L) distances were obtained from Cu K-edge XAS. The use of S K-edge XAS provided a quantitative measure for the covalent nature of Cu–S(Cys) bond[61] as expressed by the amount S 3p mixing into the Cu 3d electron–hole. The high Cu–S(Cys) covalency in blue copper proteins gives rise to the intense pre-edge feature below the S K-edge. This offered an explanation for the small $A_{||}$ in EPR[58] and rationalization of the site's electron-transfer property.[62] An additional merit of experimentally determining the Cu–S(Cys) bond covalency is the spectroscopic calibration of electronic structure methods, such as density functional theory (DFT).[40,59] In the given study, we present systematic Cu K-edge and S K-edge XANES and EXAFS studies for Met16 variants of *Ac*PAz supplemented with a complete series of hybrid DFT calculations.

When composing computational models of metal sites in proteins, the adequate treatment of outer-sphere protein environment can have a more dominant structural role[57] than selection of a given functional. In order to consider the role of the protein environment, we modeled the complete inner and first outer-shell environments of the Cu(II) site in PAz with close to 90 atoms that include key hydrogen bonding and dipole interactions imposed on the inner sphere coordination environment. Furthermore, instead of using a single hybrid functional, we utilized a series of hybrid functionals with varied amount of HF exchange (HFX) ranging 0 to 100% including the previously employed functional B38HFP86[63] for Cu(II). Therefore the reported structural changes, electronic structural features will be given as a function of the amount of HFX mixed with the density functional exchange (DFX) functional that eliminates uncertainties and bias due to use of a single density functional.

## Experimental

**Preparation of XAS Samples.** The protein samples for X-ray absorption spectroscopic measurements were expressed and purified as described before.[42,64] The copper-to-protein ratio was confirmed to be 1:1 and no zinc contamination was found by ICP-AES. The protein samples were concentrated to 5–12 mM containing 50% glycerol by ultrafiltration (3 K). Their concentrations were determined by using molecular extinction coefficients of the peak maximum around at 600 nm.[42] The samples were loaded into 100 µL Mylar cells wrapped with S and Cu contaminant free, 0.5 µm thick Kapton tape with silicon adhesive (Shercon) and stored in liquid nitrogen until measurement.

**X-ray Absorption Spectroscopy.** All XAS data were measured at Stanford Synchrotron Radiation Lightsource. The Cu K-edge XAS were collected at beam line 7-3 using a Si(220) double-crystal monochromator. The higher harmonic components were rejected by 50% detuning of the incident beam intensity. The temperature of protein samples was maintained at around 10 K during measurement using LHe cryostat (Oxford). The spectra were recorded in fluorescence mode, windowed for the Cu Kα emission line using 30 elements Ge detector (Canberra). The incident beam ($I_0$) was monitored by an Ar filled, high voltage (1.8 kV) ion chamber. The spectra of Cu foil for energy calibration were acquired simultaneously by second ($I_1$) and third ($I_2$) ion chambers.

XANES region of S K-edge were collected at SSRL beam line 4-3. The monochromatic X-ray beam was obtained by Si(110) double-crystal monochromator. The samples were cooled by a liquid He cryo-stream. The total fluorescence emission was measured using 3-element Lytle detector (EXAFS Co). The energy position of the well-resolved pre-edge feature of sodium thiosulfate pentahydrate was used for energy calibration (2472.0 eV).

**XAS Data Normalization and Fitting.** The photon energy was calibrated to the first resolved peak of the first derivative spectra for Cu-foil (8980.3 eV). The fluorescence signals from every channel of the Ge detector with useful spectra were averaged for each scan using SIXPACK.[65] The averaged data for consecutive scans were used to generate a "zero-exposure" spectrum (Supporting Information Figure S1) in order to eliminate the visible spectral shift due to radiation damage as has also been observed for X-ray spectra of redox active metalloproteins.[66–68] Background removal, normalization of edge jump, $E_0$ energy (8990 eV) definition for Cu EXAFS analysis, extraction of *k*-space oscillations and acquisition of *R*-space Fourier transform were done using Athena.[69]

The S K-edge spectra were averaged for 6, 6, and 10 scans of wild type (WT), Met16Phe, and Met16Val PAz, respectively. No signs of radiation damage were observed over these scans. Furthermore, S K-edge renormalization was carried out by considering the different number of S absorbers: 6 for WT and 5 for Met16Phe and Met16Val PAz.

**Analysis of Cu EXAFS.** The theoretical EXAFS scattering amplitudes and phase shifts for the reported crystal structure of the WT *Ac*PAz (PDB code: 1BQK)[10] were calculated using FEFF ver. 6.0.[70] Artemis was used for data fitting, interatomic distance, and Debye–Waller factor refinement. The simulation included the direct scattering pathways of Cu–N (His40 and His81), Cu–S (Cys78), multiple scattering pathways of Cu-δ-N(His)-γ/ε-C(His) and Cu-δ/ε-N(His)-γ/δ/ε-C(His), and an axial ligand of Cu–S (Met86) or Cu–O (see Results and Analysis). The axial ligand contribution to EXAFS was varied in each variant according to independent EPR[42,71] and UV/vis[44] compositions of axial and rhombic Cu sites. The degeneracy or coordination number (CN) parameter of the EXAFS equation was adjusted based on the specific "axial-to-rhombic" ratio determined in earlier,[42] (see also Supporting Information); CN = 0.95 (Met16Val), 0.83 (Met16His), 0.77 (WT), 0.67 (Met16Trp), 0.60 (Met16Tyr), and 0.45 (Met16Phe). The final fits were obtained in an iterative manner by allowing first the single scattering shells of Cu–S(Cys), average Cu–N(His), and Cu-axial ligand pathways achieve reasonable distance and Debye–Waller factors before introducing secondary single scattering pathways Cu···C(His) and lastly multiple scattering pathways for Cu···C(His)···N(His) or Cu···N(His)···C(His). Single or multiple scattering pathways involving Cu···C(Cys) did not give significant contributions to the fits and thus they were excluded from this analysis. Bond valence sum theory[72,73] was applied to connect the experimental Cu ligand distances with Cu effective nuclear charge differences from Cu K-edge XANES.

**Analysis of S XANES.** The area of pre-edge peaks for WT, Met16Phe, and Met16Val PAz were determined by fitting the renormalized spectra using PeakFit ver. 4.12. The pseudo-Voigt line shape with 1:1 Gaussian/Lorentzian mixing ratio was adopted to simulate the line-shape of the pre-edge peak of all PAz samples. The amplitude, energy position, and full-width at half maximum (FWHM) parameters were allowed to vary. The rising edge features were simulated by pseudo-Voigt line-shape with Gaussian/Lorentzian mixing ratio allowed to vary. First, the fitting of pre-edge was performed in the range of 2466–2471 eV, which was then extended in 0.5 eV steps up to 2473.5 and 2474.0 eV depending on the variant. The averaged integrated pre-edge intensities from multiple fits were used to calculate Cu–S(Cys) covalency. The transition dipole integral used for blue Cu complexes earlier[30] was scaled by 1.27 to correct for the differences between the analytical pre-edge intensities and estimated from the product of amplitude and linewidth.[74]

**EPR Spectroscopy.** X-band EPR spectra were collected on an X-Band Microwave Unit JES-FA 200 ESR SPECTROMETER (JEOL). The magnetic field was scanned between 2550 and 3550 G with the modulation amplitude of 6.3 G, at a frequency of 9.0563 GHz. The sample concentrations of protein were 1.5 mM with 100 mM potassium phosphate buffer (pH 7.0) and the temperature was maintained at 100 K during the measurement.

**Density Functional Theory Modeling.** The 89 atom computational model was generated from the 1.35 Å resolution

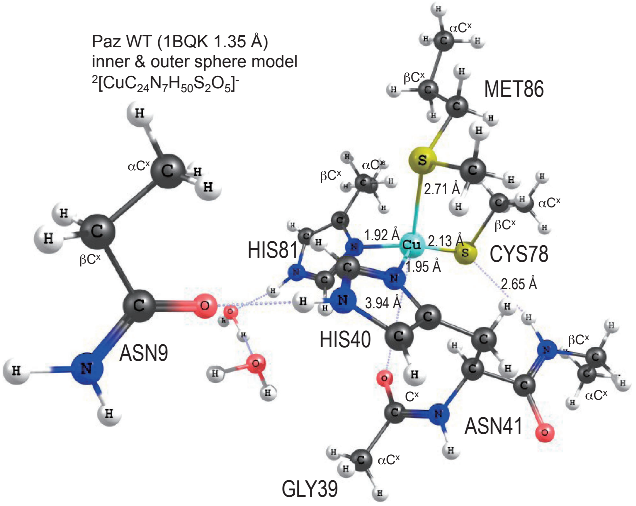

**Figure 1.** Computational model for the extended inner-sphere of the Cu site from WT PAz (1BQK[10]).

structure of WT *Ac*PAz (PDB code 1BQK[10]). The coordination environment of the Cu(II) ion was completed with inner sphere amino acids Cys78, His40, His81, and Met86 without truncation. The N- and C-terminal of each coordinated amino acid was completed with an amide moiety. In addition, two explicit solvent water molecules H-bonded to the ε-N of His40 and His81, the Gly39 with a carbonyl dipole, the Asn41 with amide H-bonding to S(Cys78), and the amide group of Asn9, were also included in the model (Figure 1). The consideration of the two water molecules at the imidazole rings and the side-chain of Asn9 was deemed to be essential to tune the nucleophilicity of the imidazole rings and thus affect the Cu–N(His) bonding as well as to provide a well rounded protein constraint around the inner sphere, respectively. Removal of the Asn9 residue allows for the backbone carbonyl to move closer to the Cu ion and form H-bonding with the proximal His ring, which is not present in the crystal structure. In addition, it tilts the entire backbone to weaken the H-bonding interaction to the thiolate sulfur. These outer sphere structural changes, in addition to the elimination of the two imidazole-bound water molecules induced significant structural changes by making the Cu coordination site more rhombic than it was found with the larger model. This structural deviation was observed with or without constraining the Cu–L distances, and the positions of the α- and β-carbon atoms of the residues. The atomic positional coordinates for the initial structure are given on the computational.chemistry.montana.edu/PAz.

The calculations were carried out using a systematic series of hybrid density functionals starting at 100% Becke DFX[75] and terminating at 100% HF exchange in 15% HFX increments with all functionals containing 100% Perdew's density functional correlation (DFC)[76] along with the Slater[77] and VWN5[78] local exchange and correlation functionals, respectively. The def2TZVP triple-ζ basis set supplemented with polarization functions[79] was used for all atoms. This was shown to correspond to the basis set saturation limit with respect to geometry, electronic structure, and energetics for Cu(II) complexes.[50] Structural optimizations were carried out using various combinations of atomic positional constraints or fixed internal coordinates, as discussed later. The Cu–N distances from the EXAFS analysis for the His coordination were differentiated as seen by crystallography by assuming 0.03 Å difference between the longer Cu–N(His40) at 1.95 Å and shorter Cu–N(His81) at 1.92 Å to give the average EXAFS Cu–N distance. Given that we were interested in stationary structures closest to the experimental WT PAz structure, no conformational analysis or frequency calculations were carried out to interrogate the stationary structures. The electrostatic effects of the protein environment was simulated by using polarizable continuum model (PCM[80]) with water solvent parameters except the dielectric constant was reduced to 10. The His ligands were solvated with explicit water molecules as seen in the crystal structure. The atomic spin densities and orbital compositions were calculated using Mulliken population analysis, since it has been shown to already provide reliable results for Cu–proteins in comparison to more advanced methods.[48]

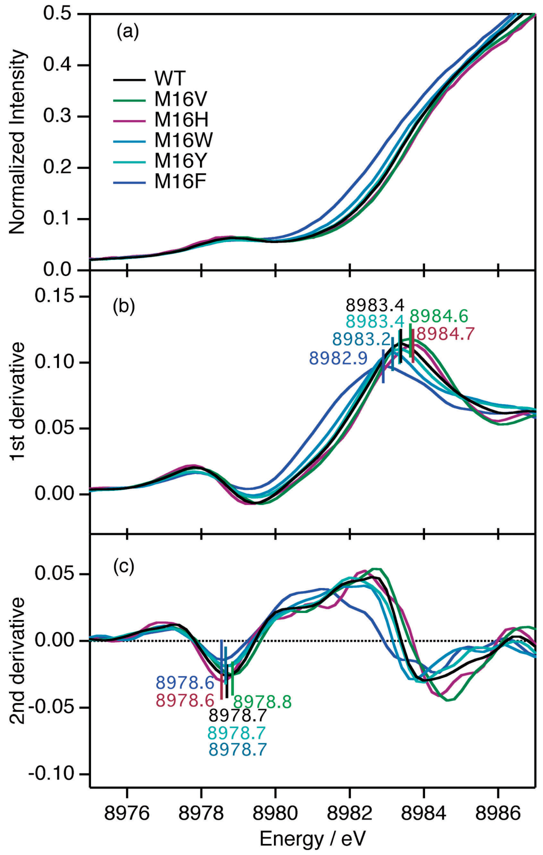

**Figure 2.** Cu K-edge XANES region (a), first (b) and second derivative spectra (c) of PAz. Bars marking first maxima of point in (b) and minima of point in (c) are indicative of effective metal oxidation state and pre-edge energy, respectively.

## Results and Discussion

**Experimental Electronic Structure of the Cu Site.** The entire range for the Cu K-edge XANES spectra for WT and Met16 variants are shown in Figure S2. The XANES region of WT and Met16 variants was found to be similar, with some notable differences. The first and second derivative spectra with pre-edge and rising-edge positions are shown in Figure 2. The

**Table 1.** Pre-edge and rising edge position of Cu K-edge XAS of WT PAz and Met16 variants relative to WT (pre-edge intensity of 0.063, energy position 8978.7 eV, rising-edge energy position 8984.4 eV)

| PAz | Pre-edge intensity | Energy/eV | Rising edge energy/eV |
|---|---|---|---|
| Met16Val | 0.001 | 0.1 | 0.2 |
| Met16His | 0.002 | −0.1 | 0.3 |
| WT | 0.000 | 0.0 | 0.0 |
| Met16Trp | −0.005 | 0.0 | −0.2 |
| Met16Tyr | −0.004 | 0.0 | 0.0 |
| Met16Phe | −0.004 | −0.1 | 0.5 |

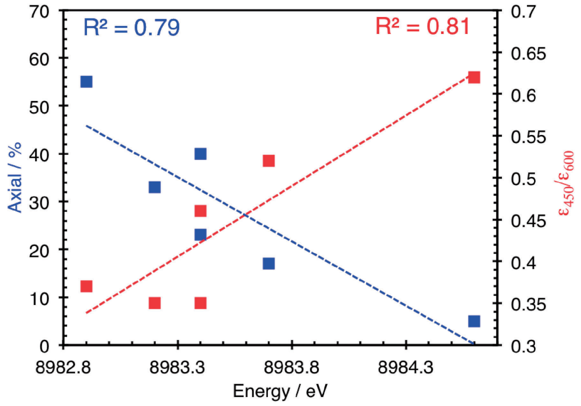

**Figure 3.** The plots of axial site population estimated from X-band EPR (left axis) and $\varepsilon_{450}/\varepsilon_{600}$ (right axis) versus rising edge energy of Cu K-edge (bottom axis).

energy positions of pre-edge features and rising edge positions are summarized in Table 1 relative to the WT. A quantitative trend for the aromatic substituents can be recognized with lower energy rising edge positions than other variants. Plotting of the axial site population[42] and $A_{450}/A_{600}$[44] against the rising-edge inflection points as a measure of Cu effective nuclear charge, $Z_{\mathrm{eff}}$(Cu) gives a notable correlation as shown in Figure 3.

**Cu Site Geometry.** The EXAFS analysis of the Cu K-edge spectra resulted in radial distribution function (RDF) in non-phase corrected dimension as shown in Figure 4. The first scattering shells around the Cu absorber were identical among the PAz variants. The $k^3$-weighted EXAFS fitting of EXAFS oscillation and RDF for the oxidized PAz are shown in Figure S3 in the Supporting Information, and the parameters are summarized in Table 2. The calculated BVS values[72,73] for pure axial and pure rhombic sites were 2.08 and 2.26, respectively, using Cu-ligand distances from Cu K-edge EXAFS. The details of the BVS calculation are provided in the Table S2. For Met16Val variant, the rhombic component was found to be the dominant (95–91%) with only 5–9% axial contribution from EPR.[42,71] Thus, the bond lengths (Cu–N(His), Cu–S(Cys), and Cu–S(Met)) of Met16Val variants were considered as those of a "pure" rhombic site. The active site of WT and other variants are mixtures of rhombic and axial sites. The most profound difference between axial and rhombic conformers is the distance between the Cu and the S(Met) centers. There is approximately 0.3 Å difference in the Cu–S(Met) distance in Pc (4DPB at 1.00 Å resolution) and NiR (2BW4 at 0.90 Å resolution). The Cu–S(Met) distances of 2.76 Å in Pc and 2.49 Å in NiR can be considered as typical values for axial and rhombic "Type 1" copper sites, whereas the Cu–L distances for other ligands are relatively similar within 0.1 Å. The presence of simultaneous presence of two different distances for a scattering pathway lowers the degree of order around the Cu absorber. Thus, the analysis of EXAFS for WT and Met16 variant excluding Met16Val becomes non-trivial. To fit the EXAFS of PAz samples in an experimentally sound manner, the coordination number of Cu–S(Met) scattering pathway was fixed to the rhombic component of each PAz from EPR.[42] The distance of the Cu–S(Met) scatterer was taken from the EXAFS fit of the Met16Val variant. Already with this simplification, the fitting was carried out successfully providing chemically meaningful results for every variant and WT PAz. The results in Table 2 show that the Cu–S(Cys) and Cu–N(His) distances were identical for all Met16 variants. The decrease in the CN value was due to the mixing of longer Cu–S(Met) distance that EXAFS measurements could not detect.[24,30,68]

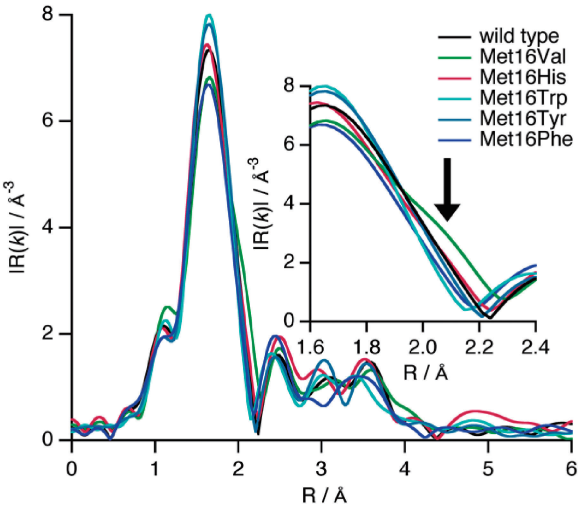

**Figure 4.** R-space spectra of Cu K-edge EXAFS region with an inset for $R = 1.6$–$2.4$ Å range. $R$ is the apparent distances.

As a control experiment, we also performed EXAFS analysis assuming the presence of an axial ligand with light atom similar to the Gly carbonyl O in Azurin (PDB code 1AZU[81]). In theory, scattering at a short distance from a light atom such as in Cu–O can result in an EXAFS scattering pattern similar to a heavy atom at a longer distance, such as the Cu–S(Met). It is important to emphasize that as expected the EXAFS fit obtained using a shorter Cu–O pathway was also acceptable for Met16Val variant (Supporting Information Figure S4); however, the possibility of O coordination can be eliminated by the X-ray crystal structure of WT PAz,[10] where the closest Cu···O distance at 3.94 Å is the carbonyl group of Gly39.

**S 3p Contribution to the Cu–S(Cys) Bond.** The pre-edge regions of S K-edge XANES spectra for WT, Met16Phe and Met16Val PAz are shown in Figure 5. The resolved pre-edge peak at around 2469 eV corresponds to S1s→LUMO excitations. The LUMO is composed of Cu $3d_{x^2-y^2}$ contribution with a combination of S(Cys) 3p and N(His) 2s/2p ligand

**Table 2.** A comparison of EXAFS fitting results of WT and Met16 variants

| Path | Degeneracy | WT | | Met16Val | | Met16His | | Met16Tyr | | Met16Trp | | Met16Phe | |
|---|---|---|---|---|---|---|---|---|---|---|---|---|---|
| | | $R$/Å | $\sigma^2$/Å$^2$ | $R$/Å | $\sigma^2$/Å$^2$ | $R$/Å | $\sigma^2$/Å$^2$ | $R$/Å | $\sigma^2$/Å$^2$ | $R$/Å | $\sigma^2$/Å$^2$ | $R$/Å | $\sigma^2$/Å$^2$ |
| Cu–N | 2 | 1.95 | 0.003 | 1.96 | 0.005 | 1.95 | 0.003 | 1.95 | 0.002 | 1.95 | 0.002 | 1.94 | 0.005 |
| Cu–$S_{Cys}$ | 1 | 2.16 | 0.002 | 2.16 | 0.002 | 2.16 | 0.003 | 2.16 | 0.003 | 2.15 | 0.003 | 2.15 | 0.003 |
| Cu–$S_{Met}$ | rhombic[a)] | 2.48 | 0.010 | 2.48 | 0.010 | 2.48 | 0.010 | 2.48 | 0.010 | 2.48 | 0.010 | 2.48 | 0.010 |
| Cu–C | 4 | 2.97 | 0.005 | 2.97 | 0.005 | 2.97 | 0.003 | 2.97 | 0.096 | 2.97 | 0.004 | 2.96 | 0.004 |
| Cu–N–C | 8 | 3.08 | 0.012 | 3.17 | 0.010 | 3.14 | 0.010 | 3.08 | 0.012 | 3.06 | 0.012 | 3.10 | 0.012 |
| Cu–N/C–N/C | 16 | 4.21 | 0.012 | 4.21 | 0.010 | 4.19 | 0.010 | 4.21 | 0.012 | 4.19 | 0.012 | 4.18 | 0.012 |

a) The coordination numbers of Cu–$S_{Met}$ were calculated from population of rhombic component estimated by X-band EPR [41]. CN = 0.77 (WT), 0.95 (Met16Val), 0.83 (Met16His), 0.60 (Met16Tyr), 0.67 (Met16Trp), and 0.45 (Met16Phe).

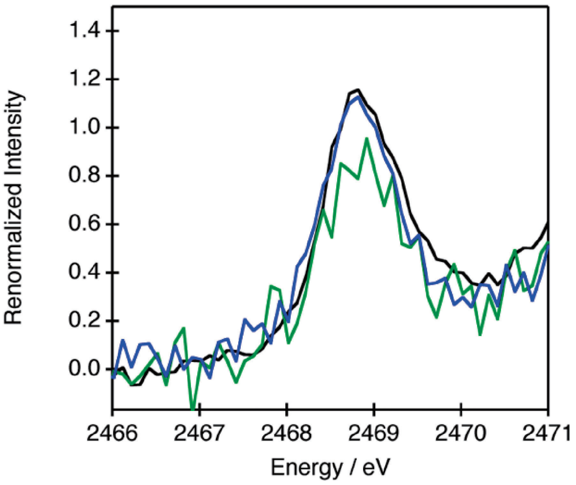

**Figure 5.** Pre-edge of WT (black), Met16Phe (blue), and Met16Val (green) in S K-edge XAS.

characters.[40] The pre-edge feature intensity (peak area) and linewidth for the renormalized spectra of WT, Met16Phe, and Met16Val PAz (Figure S5 in Supporting Information) were used to estimate the Cu–S(Cys) bond covalency to be 38 ± 3%, 39 ± 2%, and 30 ± 3% for WT, Met16Phe, and Met16Val PAz, respectively. Using these results, the Cu–S(Cys) bond covalency values for pure axial and pure rhombic site can be estimated from the S 3p characters and population of axial/rhombic[42,71] (see Supporting Information) to be approximately 49% and 31%, respectively.

**EPR Spectra of PAz.** The EPR spectra were recorded for WT and Met16His variants (Figure 6). The EPR spectrum of Met16His variants was similar to that of WT PAz with the exception of hyperfine splitting in $g_{||}$ region. The axial EPR component of Met16His was determined to be 16% according to previous estimates.[42] This value was used in the analysis of EXAFS of Met16His variants (vide supra).

**DFT Modeling of XAS Results.** **Apo Protein Models:** The amount of HF exchange in the hybrid density functional was shown to affect the description of Cu(II)–L bonding.[63] Therefore, we carried out a brief inquiry into the differences in the optimized structures of apo PAz outer-sphere models in the absence of the Cu(II) ion. Table S3 in Supporting Information shows the results for the noticeable differences between the employed functionals. The comparison of intramolecular distances within the [$N_2S_2$] tetrahedron of the Cu-coordinated atoms from the holo form revealed that the model for the apo-site changed considerably even with constrained atomic positions of the α- and β-C atoms of the amino acids. The long N···N, N···S, and S···S distances in BP86 calculations can be rationalized by the greater importance of covalent interactions and thus the shortening of bond lengths within the protein environment defined by the extended inner-sphere. In HF calculations, the long range ionic interactions become dominant and thus the bonds are allowed to expand giving rise to nearly 0.3 Å average root-mean-square deviation between HFP86 and BP86 functionals. Since the trends in geometry are monotonous in going from HFP86 to BP86, we can consider this as an artificial compression strain in pure GGA calculations on the inner sphere that expands the coordination environment of the Cu(II) site. This is an opposite trend to the observed shortening of the Cu–L distances due to the overly covalent description of pure GGA functionals. Interestingly the complete opposite is observed for the HFBP86 calculations with less covalent Cu–L distances, but still with a contracted $N_2S_2$ coordination environment.

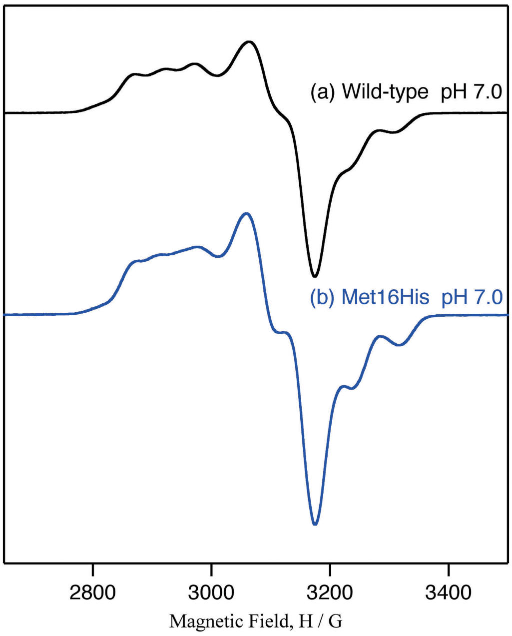

**Figure 6.** The EPR spectra of WT (black) and Met16His variants (blue) at pH 7.0.

**Holo Protein Models:** The experimental S K-edge data established a 30–39% Cu–S(Cys) bond covalency as a function of mutations and 2.16 Å Cu–S(Cys), 2.48 Å Cu–S(Met),

**Table 3.** Density functional dependence of the electronic structure of the computational model with EXAFS Cu–L constraints (Cu–S(Cys) = 2.16 Å, Cu–S(Met) = 2.48 Å, Cu–N(His) = 1.95 Å) and crystallographic α- and β-C positions considered for the WT PAz model using def2-TZVP saturated basis set

| HFX/% | $\Delta E_{\mathrm{SCF}}$[a) /kJ mol$^{-1}$ | Mulliken atomic spin densities |  |  |  |  |
|---|---|---|---|---|---|---|
|  |  | Cu | S(Cys) | S(Met) | N(His) |  |
| 0 | 4 | 0.35 | 0.42 | 0.05 | 0.09 | 0.04 |
| 15 | 3 | 0.37 | 0.47 | 0.00 | 0.07 | 0.06 |
| 30 | 3 | 0.51 | 0.31 | 0.03 | 0.09 | 0.05 |
| 38 | 4 | 0.60 | 0.23 | 0.02 | 0.08 | 0.05 |
| 45 | 4 | 0.68 | 0.17 | 0.01 | 0.08 | 0.05 |
| 60 | 5 | 0.80 | 0.09 | 0.01 | 0.07 | 0.04 |
| 75 | 6 | 0.86 | 0.05 | 0.00 | 0.05 | 0.04 |
| 100 | 7 | 0.91 | 0.03 | 0.00 | 0.04 | 0.03 |

a) Relative to the relaxed inner sphere with constraints of the positions of α- and β-C atoms.

average of 1.95 Å Cu–N(His) distances from XANES and EXAFS analysis above, respectively. The initial computational model was obtained by optimizing the crystal structure of the WT PAz with constraints of all Cu–L distances at the corresponding EXAFS values and fixing the atomic positions of α- and β-carbon atom of the considered protein backbone. Upon optimization of atoms beyond the inner-sphere, the structural changes are minimal as seen in the small energy differences (3–7 kJ mol$^{-1}$) relative to the relaxed active site structure (see below) despite the described structural changes for the apo-models. The atomic spin densities summarized in Table 3 show clearly how the covalent nature of the pure GGA functional (BP86) maximizes the spin density on the ligands, while a metal-based electronic structure obtained with the HFP86 method.

The role of the protein strain in maintaining the active site structure was estimated by structural optimizations that kept all EXAFS Cu–L constraints, but released all α- and β-C atoms. The energy stabilization upon optimization is about 35–59 kJ mol$^{-1}$ in going from BP86 to HFP86, which is a considerable energy difference. The relaxation of the protein-environment beyond the inner-sphere, conformational change in the orientation of the Cu-coordinated side-chains, while the Cu–ligand distances are fixed at their EXAFS distances, slightly perturbs the electronic structure. For example, the Cu–S(Met) bond covalency doubles (0.11 *e*) at BP86 level at the expense of the Cu–S(Cys) covalency (0.36 *e*, Table S4) in comparison to those shown in Table 3, which was found to be a trend for all functionals with gradually decreasing covalent bonding.

A critical structural feature in blue versus green copper chemistry is the position of the axial ligand. Therefore, we utilized DFT models to determine the ideal Cu–S(Met) distance within the given model in the presence of frozen α- and β-C atomic positions, fixed Cu–S(Cys), and Cu–N(His) distances at their EXAFS values. Upon optimizations, the Cu–S(Met) distances stretched from the EXAFS value of 2.48 to 2.65–2.71 Å. The range of calculated values (0.06 Å) as a function of density functional is rather small relative to the deviation (0.17–0.23 Å) from the WT structure. It is important to highlight that there is no linear trend as the BP86 and HFP86 functionals give the shortest (2.65 and 2.63 Å, respectively), while the B60HFP86 and B15HFP86 functionals provide the longest (2.68 and 2.71 Å, resp.) Cu–S(Met) distances. The elongation of the Cu–S(Met) distance and thus the trigonal distortion of the four coordinate Cu(II) site is a consequence of the reduction of the S(Met) spin density to a small 0.03 *e* value at the most covalent BP86 level.

Allowing for the relaxation of all Cu–L distances, but keeping the positions of α- and β-C atoms fixed, enabled us to evaluate how reasonable the EXAFS values are within the WT PAz protein environment as defined by the 1.35 Å resolution crystal structure. The average calculated Cu–S(Cys), Cu–S(Met), and Cu–N(His) distances are 2.19, 2.60, and 1.98 Å, respectively for all calculations. The most remarkable observation is the practically identical internal coordinates within 0.05 Å between the greatly different BP86 and HFP86 functionals. We can rationalize this by a competition between the Cu–L covalent interactions and the formally $\mathrm{Cu}^{2+}\cdots\mathrm{L}^{-/\delta-}$ ionic interactions. The less covalent HFP86 functional localizes the electron density and thus maintains the M/L charge separation closer to the formal ionic state. Large charge separation at short distances gives a comparable interaction to covalent bonding within 0.05 Å. Comparison of the EXAFS and the average calculated distances shows that our computational model and thus likely the WT PAz structure cannot accommodate both the short Cu–S(Cys) and Cu–S(Met) distances at 2.16 and 2.48 Å, respectively. The Cu–N(His) distances are within reproducibility of both the EXAFS (1.95 Å) and the crystal structure values (1.92 and 1.95 Å). It is also notable that both Cu–S distances are longer than their corresponding EXAFS values. The use of computational results for fitting the EXAFS data resulted in obvious poor fits to the experimental EXAFS as shown in Figure S3 in supporting information, which will be an important observation for the conclusion of the given study.

The correlated nature of Cu–S(Cys) bond length and the strength of axial ligand···Cu interaction have already been documented in literature.[40,59] We further substantiate this relationship at a wide range of level of theory (see Table S4) using the given computational model by shortening the Cu–S(Met) distance to the EXAFS value of 2.48 Å, while keeping the position of α- and β-C atoms fixed, but allowing the Cu–S(Cys) and Cu–N(His) bond lengths to vary. With every functional, the releasing of the Cu–S(Cys) and Cu–N(His) distances while keeping the Cu–S(Met) distance at 2.48 Å results in Cu–S(Cys) distances that vary between 2.19 and 2.25 Å relative to the EXAFS value of 2.16 Å. Furthermore, the Cu–N(His)

**Table 4.** Result of fully relaxed structural optimizations for the extended inner-sphere model of Cu(II) in WT PAz

| HFX/% | $\Delta E_{\text{SCF}}$ /kJ mol$^{-1}$ | Mulliken atomic spin densities | | | | | Cu(II)–L distances | | | |
|---|---|---|---|---|---|---|---|---|---|---|
| | | Cu | S(Cys) | S(Met) | N(His) | | S(Cys) | S(Met) | N(His) | |
| 0 | −41 | 0.34 | 0.37 | 0.14 | 0.06 | 0.04 | 2.24 | 2.38 | 2.04 | 2.04 |
| 15 | −62 | 0.40 | 0.34 | 0.12 | 0.07 | 0.04 | 2.23 | 2.38 | 2.04 | 2.04 |
| 30 | −43 | 0.51 | 0.26 | 0.10 | 0.07 | 0.05 | 2.23 | 2.40 | 2.02 | 2.03 |
| 38 | −61 | 0.62 | 0.22 | 0.02 | 0.08 | 0.05 | 2.23 | 2.42 | 2.01 | 2.02 |
| 45 | −43 | 0.71 | 0.16 | 0.01 | 0.08 | 0.05 | 2.23 | 2.43 | 2.00 | 2.01 |
| 60 | −63 | 0.80 | 0.07 | 0.03 | 0.06 | 0.04 | 2.25 | 2.47 | 1.99 | 1.99 |
| 75 | −48 | 0.86 | 0.04 | 0.02 | 0.04 | 0.04 | 2.25 | 2.48 | 1.99 | 1.99 |
| 100 | −59 | 0.91 | 0.02 | 0.01 | 0.03 | 0.03 | 2.26 | 2.50 | 1.98 | 1.98 |

distances vary 1.97–2.01 Å relative to 1.95 Å from experimental structure. The shorter Cu–S(Met) distance increases the spin density at the S(Met) up to 0.06 *e*, which is already in an experimentally detectable range for EPR or XAS. The elongation of the Cu–S(Met) distance to a value more typical (2.8 Å) for axially distorted tetragonal blue Cu sites in Pc[40,59] reduces the Cu–S(Cys) distance to 2.16–2.22 Å with the Cu–N(His) distances being at around 1.95–1.99 Å. This is a further confirmation of the coupled behavior of the two S ligands. Release of the constrained Cu–S(Met) distance returns all structure to the exact same position as obtained from releasing the initial model with EXAFS and crystallographic constraints.

For evaluating the combined effects of all protein strain via the constrained coordinates of α- and β-C positions or Cu–L EXAFS constraints, we carried out full optimization for an extended inner-sphere environment. The optimization results in Table 4 show that there is only one global minima for the Cu(II) site in cupredoxins, which is the tetragonally distorted tetrahedral coordination environment regardless of the starting structure and the composition of hybrid density functional. Upon relaxation of all constraints, the Cu–S(Met) distance becomes short (2.38–2.50 Å) with 0.14–0.01 *e* spin density accumulation at the S(Met) center. This is a direct indication of covalent Cu–S(Met) bonding, which is only possible upon tetragonal rhombic distortion. This was achieved at the expense of Cu–S(Cys) distance and S(Cys) spin density that became long (2.24–2.26 Å) and small (0.37–0.02 *e*), respectively. The Cu–N(His) distances elongates as well by 0.03–0.09 Å, but their spin densities do not vary significantly.

## Discussion

A multi-edge XAS study on WT, Met16Val, His, Tyr, Trp, and Phe variants of PAz allowed for the simultaneous experimental analysis of Cu and S electronic structures and metal–ligand distances. The smaller energy shift of the rising edge energy in Cu XANES showed correlation with the increased axial component for the "Type 1" copper site. This indicates a more reduced Cu site for the axial structure than for the rhombic, which is opposite to that expected. This was further elaborated by the difference of bond valence sum[72,73] giving lower valence number for the axial than for the rhombic site. XAS results suggest that a more covalent Cu–S(Cys) π bonding is present in the axial site than that of the combined covalent effect of the pseudo-σ bonding in Cu–S(Cys) and Cu–S(Met) in the rhombic site. The contributions from the Cu–N bonds are expected to be comparable in both blue and green sites. The Cu K-edge EXAFS showed similar Cu–ligand distances for each Met16 variant independent of the axial-to-rhombic ratio as a function of mutation. The maximum difference in Cu–N(His) and Cu–S(Cys) distances among the studied Met16 variants were 0.02 and 0.01 Å, respectively. These negligible variations suggest that the axial and rhombic sites are identical with respect to the Cu–L distances in basal plane. Given that the axial site was found to be more covalent, and thus has a more reduced Cu site with less ionic bonding between Cu and ligands (especially for thiolate S) relative to the rhombic site, the combined effect of ionic and covalent interactions minimizes the bond length differences. This effect has been computationally modeled by the use of a series of hybrid functionals with varied amount of ionic HF exchange. For example, the calculated Cu–S(Cys) distance varies between 2.23 and 2.26 Å (only within 0.03 Å) while the S covalency range from 2% to 37%.

The Cu–S(Met) distance refined to 2.48 Å from EXAFS of Met16Val PAz is responsible for the presence of the rhombic structure. The decreasing contribution of Cu–S(Met) scattering pathway detected by EXAFS as a result of increasing axial component based on EPR suggests that the Cu–S(Met) distance in the axial site is considerably longer than 2.48 Å. It is of a distance that cannot be detected by EXAFS.

Analyses of pre-edge features at the S K-edge defined the Cu–S(Cys) bond covalency for WT and Met16Phe and Met16Val variants to be 38, 39, and 30% S 3p character, respectively. The bond covalency of pure axial and pure rhombic sites was estimated using the axial-to-rhombic ratios of PAz from EPR measurements. The covalency for a pure axial site in PAz (49%) is in agreement with that of Gln99Met stellacyanin variant (48%).[30]

In order to relate the results of Cu and S XAS and translate those into structural information, DFT modeling was carried out using the crystal structure of WT PAz (1BQK). Instead of using a single functional, we employed a range of hybrid functionals from the pure GGA to the hybrid GGA with 100% HF exchange. The range of hybrid functionals covered bonding scenarios with an overly covalent electronic structure (pure GGA functions), a spectroscopically calibrated (B38HFP86), and a localized ionic structure (100% HF with GGA correlation functional). We found that the role of ionic interactions in determining the Cu site geometry is equally important to the covalent interactions. Structural optimizations showed the interconnectedness of Cu–S(Cys) and Cu–S(Met) bonds that are critical in determining the Cu site coordination geometry. The Cu–N(His) bonds showed only limited variability between the axial and rhombic sites. In addition to the distances, the spin densities at the atoms of ligands directly bound to the Cu also manifest differences depending on whether the Cu has axial versus rhombic geometry. In the rhombic site, the Cu–S(Cys) bond covalency decreases considerably at the benefit of the covalent character of the Cu–S(Met) bond. This change was also detected by the S K-edge XAS measurements. We attempted to obtain experimental information for Cu–S(Met) covalency; however, the corresponding spectral features are under the rising-edge of the S K-edge and they could not be reliably investigated by using a protein sample mimicking mixture of Cys and Met residues.

The Cu coordination environment turned out to be pliable energetically regardless of the employed functional. There are only a few $\mathrm{kJ\,mol^{-1}}$ energy differences between the relaxed and the EXAFS constrained inner sphere structure. Relaxation of the protein-strain as modeled by the fixed positions of α- and β-C atoms generates a considerable energy stabilization for the Cu site of about 41–64 $\mathrm{kJ\,mol^{-1}}$. This is in the same order of magnitude to the decrease of the inner sphere reorganization energy experimentally estimated by Gray et al. ($\lambda_{\mathrm{inner}}$ from 2.4 eV for $\mathrm{Cu(phen)_2}^{2+/+}$ to 0.6–0.8 eV for azurin)[18,82] or calculated protein strain energy by Ryde et al. (ca. 30 $\mathrm{kJ\,mol^{-1}}$).[83] Relaxation of all constrained optimizations resulted in a single Cu inner sphere structure regardless of the initial structure and the employed hybrid GGA functional. This structure corresponds to elongated Cu–S(Cys) and short Cu–S(Met) distances with an overall rhombic structure.

## Conclusion

The combined XAS, EPR, and DFT study probed the possibility for the presence of multiple Cu coordination environments for a series of Met16 variants of PAz with distinct spectral features and electronic structural properties. Our results extend the previous studies on blue and green Cu proteins by drawing attention to the structural influence of amino acid mutations in the second coordination sphere on the immediate ligand environment of the Cu site. The site of mutation (16th amino acid) was consciously chosen from comparisons of fern versus higher plant plastocyanin structures.[42] Our results hint the possibility for additional structural roles for this particular position than direct perturbation of the Cu site through outer sphere interactions. A 90-atom computational model with an extended inner-sphere protein environment to the Cu site from the WT PAz did not reproduce the Cu K-edge EXAFS results regardless of using a realistic model and a wide range of hybrid density functionals. Furthermore, the use of optimized structures as input for Cu K-edge EXAFS analysis did not result in acceptable fits. This suggests that the protein environment outside of the considered first- and second-shell environments needs to be responsible for the inner sphere coordination geometry changes.

A protein strain-based mechanism is assumed to be acting here, which compacts the active site to have short Cu–S(Met) as well as short Cu–S(Cys) distances and a rhombic coordination environment. The movement of residues in the second coordination sphere to the Cu site can originate from protein dynamics. This can change the tertiary structure as a result of allosteric effects. This brings up the possibility for Cu being only a spectator ion in “Type 1” cupredoxins, which responds to even longer range protein structural perturbations than just first and second coordination sphere. The Jahn–Teller distortion force could then be overcome by protein-strain effects that set the Cu coordination geometry to be axial rather than a rhombic. Therefore the two different “Type 1” Cu site states are not exclusive, but they can coexist within the same protein as resulting from protein dynamics involving outer sphere environment of the Cu site. Thus, we conclude that changes in the protein environment due to the variation of weak interaction from 16th amino acid can be responsible for geometric/electronic structure variations and the emergence of different spectroscopic/electrochemical properties of “Type 1” copper site. Spectroscopic (temperature dependent EPR), biochemical (pH, counter ion effects on the $A_{450}/A_{600}$ ratios), and computational (systematic perturbation of amino acid backbone positions) studies are underway to provide comprehensive support for the presence of allosteric effects in blue and green-Cu proteins.

This work has been supported by the JSPS (No. 22550145 to TK), NSF (No. 0744820 to RKS) and Sekisho Scholar Award (TY). Portions of this research were conducted at the Stanford Synchrotron Radiation Laboratory (SSRL) BL 7-3 and BL 4-3, a national user facility operated by Stanford University on behalf of the U.S. Department of Energy, Office of Basic Energy Sciences. The SSRL Structural Molecular Biology Program is supported by the Department of Energy, Office of Biological and Environmental Research, and by the National Institutes of Health, National Center for Research Resources, Biomedical Technology Program, and the National Institute of General Medical Sciences.

## Supporting Information

The X-ray absorption spectroscopic data (Figures S1, S2, S3, S4, S5, S6, S7, and S8 and Tables S1 and S2) and DFT data (Tables S3 and S4) are available electronically on J-STAGE.

## References

1 C. Dennison, *Coord. Chem. Rev.* **2005**, *249*, 3025.

2 B. G. Malmström, B. Reinhammar, T. Vänngård, *Biochim. Biophys. Acta, Bioenerg.* **1970**, *205*, 48.

3 A. Marchesini, M. Minelli, H. Merkle, P. M. H. Kroneck, *Eur. J. Biochem.* **1979**, *101*, 77.

4 O. Einsle, Z. Mehrabian, R. Nalbandyan, A. Messerschmidt, *J. Biol. Inorg. Chem.* **2000**, *5*, 666.

5 P. M. Colman, H. C. Freeman, J. M. Guss, M. Murata, V. A. Norris, J. A. M. Ramshaw, M. P. Venkatappa, *Nature* **1978**, *272*, 319.

6 E. W. Ainscough, A. G. Bingham, A. M. Brodie, W. R. Ellis, H. B. Gray, T. M. Loehr, J. E. Plowman, G. E. Norris, E. N. Baker, *Biochemistry* **1987**, *26*, 71.

7 J. Tobari, Y. Harada, *Biochem. Biophys. Res. Commun.* **1981**, *101*, 502.

8 J. T. Trost, J. D. McManus, J. C. Freeman, B. L. Ramakrishna, R. E. Blankenship, *Biochemistry* **1988**, *27*, 7858.

9 E. I. Solomon, M. D. Lowery, *Science* **1993**, *259*, 1575.

10 T. Inoue, N. Nishio, S. Suzuki, K. Kataoka, T. Kohzuma, Y. Kai, *J. Biol. Chem.* **1999**, *274*, 17845.

11 S. Najmudin, S. R. Pauleta, I. Moura, M. J. Romão, *Acta Crystallogr., Sect. F: Struct. Biol. Cryst. Commun.* **2010**, *66*, 627.

12 T. Inoue, M. Gotowda, H. Sugawara, T. Kohzuma, F. Yoshizaki, Y. Sugimura, Y. Kai, *Biochemistry* **1999**, *38*, 13853.

13 T. Inoue, H. Sugawara, S. Hamanaka, H. Tsukui, E. Suzuki, T. Kohzuma, Y. Kai, *Biochemistry* **1999**, *38*, 6063.

14 P. J. Hart, D. Eisenberg, A. M. Nersissian, J. S. Valentine, R. G. Herrmann, R. M. Nalbandyan, *Protein Sci.* **1996**, *5*, 2175.

15 C. Li, T. Inoue, M. Gotowda, S. Suzuki, K. Yamaguchi, K. Kataoka, Y. Kai, *Acta Crystallogr., Sect. D: Biol. Crystallogr.* **1998**, *54*, 347.

16 S. V. Antonyuk, R. W. Strange, G. Sawers, R. R. Eady, S. S. Hasnain, *Proc. Natl. Acad. Sci. U.S.A.* **2005**, *102*, 12041.

17 G. S. Kachalova, A. C. Shosheva, G. P. Bourenkov, A. A. Donchev, M. I. Dimitrov, H. D. Bartunik, *J. Inorg. Biochem.* **2012**, *115*, 174.

18 H. B. Gray, B. G. Malmström, R. J. P. Williams, *J. Biol. Inorg. Chem.* **2000**, *5*, 551.

19 T. Inoue, Y. Kai, S. Harada, N. Kasai, Y. Ohshiro, S. Suzuki, T. Kohzuma, J. Tobari, *Acta Crystallogr., Sect. D: Biol. Crystallogr.* **1994**, *50*, 317.

20 Y. Xie, T. Inoue, Y. Miyamoto, H. Matsumura, K. Kataoka, K. Yamaguchi, M. Nojini, S. Suzuki, Y. Kai, *J. Biochem.* **2005**, *137*, 455.

21 I. Zaitseva, V. Zaitsev, G. Card, K. Moshkov, B. Bax, A. Ralph, P. Lindley, *J. Biol. Inorg. Chem.* **1996**, *1*, 15.

22 V. Ducros, A. M. Brzozowski, K. S. Wilson, P. Østergaard, P. Schneider, A. Svendson, G. J. Davies, *Acta Crystallogr., Sect. D: Biol. Crystallogr.* **2001**, *57*, 333.

23 M. D. Lowery, E. I. Solomon, *Inorg. Chim. Acta* **1992**, *198–200*, 233.

24 S. DeBeer, D. W. Randall, A. M. Nersissian, J. S. Valentine, B. Hedman, K. O. Hodgson, E. I. Solomon, *J. Phys. Chem. B* **2000**, *104*, 10814.

25 N. Bonander, B. G. Karlsson, T. Vänngård, *Biochemistry* **1996**, *35*, 2429.

26 S. M. Berry, M. Ralle, D. W. Low, N. J. Blackburn, Y. Lu, *J. Am. Chem. Soc.* **2003**, *125*, 8760.

27 D. K. Garner, M. D. Vaughan, H. J. Hwang, M. G. Savelieff, S. M. Berry, J. F. Honek, Y. Lu, *J. Am. Chem. Soc.* **2006**, *128*, 15608.

28 L. Basumallick, R. K. Szilagyi, Y. Zhao, J. P. Shapleigh, C. P. Scholes, E. I. Solomon, *J. Am. Chem. Soc.* **2003**, *125*, 14784.

29 J. W. A. Coremans, O. G. Poluektov, E. J. J. Groenen, G. C. M. Warmerdam, G. W. Canters, H. Nar, A. Messerschmidt, *J. Phys. Chem.* **1996**, *100*, 19706.

30 S. DeBeer George, L. Basumallick, R. K. Szilagyi, D. W. Randall, M. G. Hill, A. M. Nersissian, J. S. Valentine, B. Hedman, K. O. Hodgson, E. I. Solomon, *J. Am. Chem. Soc.* **2003**, *125*, 11314.

31 B. G. Karlsson, R. Aasa, B. G. Malmström, L. G. Lundberg, *FEBS Lett.* **1989**, *253*, 99.

32 A. E. Palmer, R. K. Szilagyi, J. R. Cherry, A. Jones, F. Xu, E. I. Solomon, *Inorg. Chem.* **2003**, *42*, 4006.

33 M. H. M. Olsson, U. Ryde, *J. Biol. Inorg. Chem.* **1999**, *4*, 654.

34 H. Li, S. P. Webb, J. Ivanic, J. H. Jensen, *J. Am. Chem. Soc.* **2004**, *126*, 8010.

35 A. G. Sykes, *Chem. Soc. Rev.* **1985**, *14*, 283.

36 E. L. Gross, *Photosynth. Res.* **1993**, *37*, 103.

37 B. A. Averill, *Chem. Rev.* **1996**, *96*, 2951.

38 T. Kohzuma, S. Shidara, S. Suzuki, *Bull. Chem. Soc. Jpn.* **1994**, *67*, 138.

39 L. B. LaCroix, S. E. Shadle, Y. Wang, B. A. Averill, B. Hedman, K. O. Hodgson, E. I. Solomon, *J. Am. Chem. Soc.* **1996**, *118*, 7755.

40 E. I. Solomon, R. K. Szilagyi, S. DeBeer George, L. Basumallick, *Chem. Rev.* **2004**, *104*, 419.

41 A. Takashina, M. Unno, T. Kohzuma, *Chem. Lett.* **2015**, *44*, 268.

42 R. F. Abdelhamid, Y. Obara, Y. Uchida, T. Kohzuma, D. M. Dooley, D. E. Brown, H. Hori, *J. Biol. Inorg. Chem.* **2007**, *12*, 165.

43 S. Yanagisawa, P. B. Crowley, S. J. Firbank, A. T. Lawler, D. M. Hunter, W. McFarlane, C. Li, T. Kohzuma, M. J. Banfield, C. Dennison, *J. Am. Chem. Soc.* **2008**, *130*, 15420.

44 M. B. Fitzpatrick, Y. Obara, K. Fujita, D. E. Brown, D. M. Dooley, T. Kohzuma, R. S. Czernuszewicz, *J. Inorg. Biochem.* **2010**, *104*, 250.

45 D. M. Dooley, R. S. Moog, M.-Y. Liu, W. J. Payne, J. LeGall, *J. Biol. Chem.* **1988**, *263*, 14625.

46 U. Ryde, M. H. M. Olsson, K. Pierloot, B. O. Roos, *J. Mol. Biol.* **1996**, *261*, 586.

47 P. Comba, V. Müller, R. Remenyi, *J. Inorg. Biochem.* **2004**, *98*, 896.

48 R. K. Szilagyi, E. I. Solomon, *Curr. Opin. Chem. Biol.* **2002**, *6*, 250.

49 S. Ghosh, X. Xie, A. Dey, Y. Sun, C. P. Scholes, E. I. Solomon, *Proc. Natl. Acad. Sci. U.S.A.* **2009**, *106*, 4969.

50 X. Xie, R. G. Hadt, S. R. Pauleta, P. J. González, S. Un, I. Moura, E. I. Solomon, *J. Inorg. Biochem.* **2009**, *103*, 1307.

51 E. I. Solomon, R. G. Hadt, *Coord. Chem. Rev.* **2011**, *255*, 774.

52 M. C. Machczynski, H. B. Gray, J. H. Richards, *J. Inorg. Biochem.* **2002**, *88*, 375.

53 C. W. Hoitink, G. W. Canters, *J. Biol. Chem.* **1992**, *267*, 13836.

54 T. Kohzuma, T. Inoue, F. Yoshizaki, Y. Sasakawa, K. Onodera, S. Nagatomo, T. Kitagawa, S. Uzawa, Y. Isobe, Y. Sugimura, M. Gotowda, Y. Kai, *J. Biol. Chem.* **1999**, *274*, 11817.

55 G. Bunker, *Introduction to XAFS: A Practical Guide to X-ray Absorption Fine Structure Spectroscopy*, Cambridge University Press, **2010**.

56 S. DeBeer, P. Wittung-Stafshede, J. Leckner, G. Karlsson, J. R. Winkler, H. B. Gray, B. G. Malmström, E. I. Solomon, B. Hedman, K. O. Hodgson, *Inorg. Chim. Acta* **2000**, *297*, 278.

57 R. Sarangi, S. I. Gorelsky, L. Basumallick, H. J. Hwang, R. C. Pratt, T. D. P. Stack, Y. Lu, K. O. Hodgson, B. Hedman, E. I. Solomon, *J. Am. Chem. Soc.* **2008**, *130*, 3866.

58 S. E. Shadle, J. E. Penner-Hahn, H. J. Schugar, B. Hedman, K. O. Hodgson, E. I. Solomon, *J. Am. Chem. Soc.* **1993**, *115*, 767.

59 E. I. Solomon, B. Hedman, K. O. Hodgson, A. Dey, R. K. Szilagyi, *Coord. Chem. Rev.* **2005**, *249*, 97.

60 M. L. Barrett, I. Harvey, M. Sundararajan, R. Surendran, J. F. Hall, M. J. Ellis, M. A. Hough, R. W. Strange, I. H. Hillier, S. S. Hasnain, *Biochemistry* **2006**, *45*, 2927.

61 T. Glaser, B. Hedman, K. O. Hodgson, E. I. Solomon, *Acc. Chem. Res.* **2000**, *33*, 859.

62 M. D. Lowery, J. A. Guckert, M. S. Gebhard, E. I. Solomon, *J. Am. Chem. Soc.* **1993**, *115*, 3012.

63 R. K. Szilagyi, M. Metz, E. I. Solomon, *J. Phys. Chem. A* **2002**, *106*, 2994.

64 S. Yanagisawa, K. Sato, M. Kikuchi, T. Kohzuma, C. Dennison, *Biochemistry* **2003**, *42*, 6853.

65 S. M. Webb, *Phys. Scr.* **2005**, 1011.

66 J. Yano, V. K. Yachandra, *Photosynth. Res.* **2009**, *102*, 241.

67 G. N. George, I. J. Pickering, M. J. Pushie, K. Nienaber, M. J. Hackett, I. Ascone, B. Hedman, K. O. Hodgson, J. B. Aitken, A. Levina, C. Glover, P. A. Lay, *J. Synchrotron Radiat.* **2012**, *19*, 875.

68 J. E. Penner-Hahn, M. Murata, K. O. Hodgson, H. C. Freeman, *Inorg. Chem.* **1989**, *28*, 1826.

69 B. Ravel, M. Newville, *J. Synchrotron Radiat.* **2005**, *12*, 537.

70 J. J. Rehr, R. C. Albers, *Rev. Mod. Phys.* **2000**, *72*, 621.

71 P. Gast, F. G. J. Broeren, S. Sottini, R. Aoki, A. Takashina, T. Yamaguchi, T. Kohzuma, E. J. J. Groenen, *J. Inorg. Biochem.* **2014**, *137*, 57.

72 W. Liu, H. H. Thorp, *Inorg. Chem.* **1993**, *32*, 4102.

73 H. H. Thorp, *Inorg. Chem.* **1992**, *31*, 1585.

74 L. J. Giles, A. Grigoropoulos, R. K. Szilagyi, *J. Phys. Chem. A* **2012**, *116*, 12280.

75 A. D. Becke, *Phys. Rev. A* **1988**, *38*, 3098.

76 J. P. Perdew, Y. Wang, *Phys. Rev. B* **1992**, *45*, 13244.

77 J. C. Slater, *The Self-consistent Field for Molecules and Solids*, **1974**, McGraw-Hill, New York.

78 S. H. Vosko, L. Wilk, M. Nusair, *Can. J. Phys.* **1980**, *58*, 1200.

79 A. Schäfer, C. Huber, R. Ahlrichs, *J. Chem. Phys.* **1994**, *100*, 5829.

80 J. Tomasi, B. Mennucci, R. Cammi, *Chem. Rev.* **2005**, *105*, 2999.

81 E. T. Adman, L. H. Jensen, *Isr. J. Chem.* **1981**, *21*, 8.

82 J. R. Winkler, P. Wittung-Stafshede, J. Leckner, B. G. Malmström, H. B. Gray, *Proc. Natl. Acad. Sci. U.S.A.* **1997**, *94*, 4246.

83 U. Ryde, M. H. M. Olsson, *Int. J. Quantum Chem.* **2001**, *81*, 335.